RESEARCH METHODS

Kilohertz electron paramagnetic resonance spectroscopy of single nitrogen centers at zero magnetic field

Fei Kong[1,2,3]*, Pengju Zhao[1,2,3]*, Pei Yu[1,2,3]*, Zhuoyang Qin[1,2,3], Zhehua Huang[1,2,3], Zhecheng Wang[1,2,3], Mengqi Wang[1,2,3], Fazhan Shi[1,2,3]†, Jiangfeng Du[1,2,3]†

Electron paramagnetic resonance (EPR) spectroscopy is among the most important analytical tools in physics, chemistry, and biology. The emergence of nitrogen-vacancy (NV) centers in diamond, serving as an atomic-sized magnetometer, has promoted this technique to single-spin level, even under ambient conditions. Despite the enormous progress in spatial resolution, the current megahertz spectral resolution is still insufficient to resolve key heterogeneous molecular information. A major challenge is the short coherence times of the sample electron spins. Here, we address this challenge by using a magnetic noise–insensitive transition between states of different symmetry. We demonstrate a 27-fold narrower spectrum of single substitutional nitrogen (P1) centers in diamond with a linewidth of several kilohertz, and then some weak couplings can be resolved. Those results show both spatial and spectral advances of NV center–based EPR and provide a route toward analytical (EPR) spectroscopy at the single-molecule level.

INTRODUCTION

Electron paramagnetic resonance (EPR) spectroscopy, a technique for studying paramagnetic targets, is an indispensable component of magnetic resonance spectroscopy for investigations of molecular structures and fast dynamics (*1*). An important goal of this technique is to extract precise information from small-volume samples (*2*), which requires both high spatial and high spectral resolution. In the past decades, intensive efforts have been devoted to promote the spatial resolution, and ultimately, single-spin EPR has been realized by various approaches, such as magnetic resonance force microscopy (*3*), scanning tunneling microscopy (*4*), and nitrogen-vacancy (NV) center–based EPR spectroscopy (*5*–*7*). Among them, the NV center is more promising for biological applications because of the compatibility with ambient conditions (*5*–*7*). However, the current spectral resolution of those techniques is on the orders of megahertz (*3*–*12*). It is insufficient to resolve molecules of slightly different structures (*13*) or local polarity profiles (*14*). For example, the distance between paramagnetic centers studied by EPR techniques is in the range of 1.8 to 6 nm (*15*), corresponding to the dipolar coupling strength of megahertz to submegahertz, the variations of which induced by conformation changes will be even smaller.

The line broadening is generally attributed to the limited spin-state lifetime of sensors and the decoherence of target spins. The former one has recently been overcome by using quantum memories (*16*, *17*). The latter, which is more fundamental (*18*), arises from the magnetic couplings to bath spins. To address spin decoherence, a simple but powerful strategy is the use of particular spin states that are naturally insensitive to external perturbations. This phenomenon exists in various physical systems, for example, so-called "clock transitions" in trapped ions (*19*, *20*) and phosphorus donors in silicon (*21*, *22*), or transitions between long-lived states in nuclear spin resonance spectroscopy (*18*, *23*). The line-narrowing phenomenon has also been found long ago in conventional zero-field EPR spectroscopy (*24*–*26*). Nonetheless, the detection via inductive pickup suffers from the very small thermal polarization at zero field and thus requires a large amount of samples (*27*), which prevents practical applications of zero-field EPR. Fortunately, the NV center is a good magnetic sensor at zero magnetic field (*28*). In a previous study (*12*), we have found that the NV center is a promising sensor for zero-field EPR without loss of sensitivity, because the statistical fluctuations of the spin polarization, which do not depend on the magnetic field, dominate in its nanoscale detection volumes rather than thermal polarization.

Here, we show that the magnetic noise–insensitive transition can be observed by a single NV center. To investigate the spectral figure, we develop a correlation method for zero-field EPR spectroscopy. We demonstrate the high-resolution nature on single substitutional nitrogen centers (P1 centers) in diamond, which are electron spins with coupling to ^{15}N nuclear spins. The linewidth of the observed spectra is as narrow as 8.6 kHz, which is a 27-fold improvement compared with the ordinary spectrum. Our results show not only the spatial but also the spectral advances of NV centers in EPR detections.

RESULTS

Magnetic noise–insensitive transition at zero magnetic field

Our model consists of an optically probed NV center and a dark electron spin (Fig. 1A), which serve as the magnetic sensor and the target, respectively. In general, the target spin can be any spin-half electron spins ($S = 1/2$) with hyperfine coupling to a nearby spin half-integer nuclear spin ($I = n/2$). For simplicity, here we take the $S = 1/2$, $I = 1/2$ system as an example. At zero magnetic field, the spin Hamiltonian of this electron-nuclei system is determined solely by the hyperfine interaction and can be written as (*24*)

$$H_0 = A_\perp(S_x I_x + S_y I_y) + A_\parallel S_z I_z \quad (1)$$

[1]Hefei National Laboratory for Physical Sciences at the Microscale and Department of Modern Physics, University of Science and Technology of China, Hefei 230026, China. [2]CAS Key Laboratory of Microscale Magnetic Resonance, University of Science and Technology of China, Hefei 230026, China. [3]Synergetic Innovation Center of Quantum Information and Quantum Physics, University of Science and Technology of China, Hefei 230026, China.
*These authors contributed equally to this work.
†Corresponding author. Email: fzshi@ustc.edu.cn (F.S.); djf@ustc.edu.cn (J.D.)

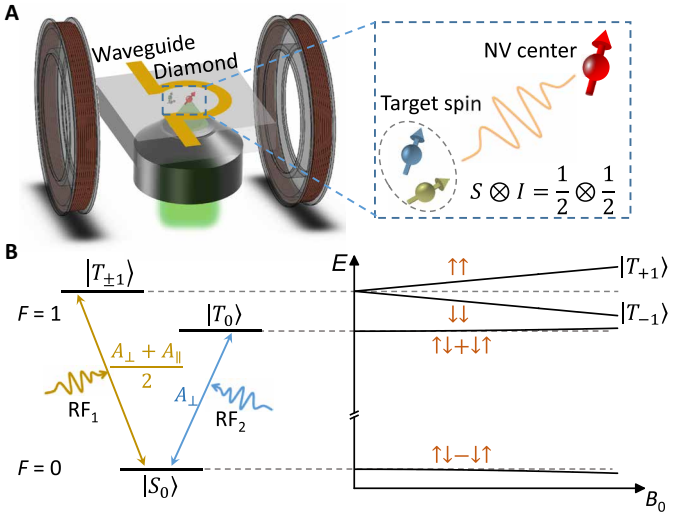

Fig. 1. Schematic representation of the NV center–based zero-field EPR spectrometer. (**A**) Geometry of the experimental setup. The sensor is a shallow NV center in diamond, which is observed by a confocal microscope with green laser excitation and red fluorescence collection. The Ω-shape waveguide radiates microwave and radio frequency (RF) to control the sensor and the target. The three-dimensional Helmholtz coils (only one of them is represented) are used to compensate for residual magnetic fields. The inset gives our model, where the target consists of a spin-1/2 electron spin and a spin-1/2 nuclear spin. (**B**) Energy levels of the target spin. The degeneracy of $|T_{\pm1}\rangle$ is lifted by a magnetic field B_0 with a linearly dependent splitting, while $|S_0\rangle$ and $|T_0\rangle$ have zero first-order dependence on B_0. The $ST_{\pm1}$ and ST_0 transitions can be driven by perpendicular RF_1 and parallel RF_2 pulses, respectively (section S1). Up/down arrows denote the high-field spin-up/down states.

where $A_\perp$ and $A_\parallel$ are the hyperfine constants. The eigenstates consist of one antisymmetric singlet $|S_0\rangle$ with $F = 0$ and three symmetric triplet states $|T_0\rangle$ and $|T_{\pm1}\rangle$ with $F = 1$, where $\mathbf{F} = \mathbf{S} + \mathbf{I}$ is the total angular momentum. The corresponding eigenvalues are

$$\omega_{S_0} = -\frac{A_\perp}{2} - \frac{A_\parallel}{4},$$
$$\omega_{T_0} = \frac{A_\perp}{2} - \frac{A_\parallel}{4}, \quad (2)$$
$$\omega_{T_{\pm1}} = \frac{A_\parallel}{4}$$

In the presence of magnetic noise $\delta\mathbf{b}$, the energy levels of the target spin will fluctuate, leading to line broadening. It can be described by a perturbation to the Hamiltonian

$$\delta H = \sum_{j=x,y,z} \delta_j S_j \quad (3)$$

where $\delta_j = \gamma_e \cdot \delta b_j$, with γ_e being the gyromagnetic ratio of the electron spin. Here, we ignore the Zeeman terms of the nuclear spin because of the nearly three orders of magnitude smaller gyromagnetic ratio than electron spins. According to the perturbation theory, the energy level shifts can be simplified as (section S1)

$$\delta\omega_{S_0} \approx -\frac{\delta_x^2 + \delta_y^2}{2(A_\parallel + A_\perp)} - \frac{\delta_z^2}{4A_\perp},$$
$$\delta\omega_{T_0} \approx -\frac{\delta_x^2 + \delta_y^2}{2(A_\parallel - A_\perp)} + \frac{\delta_z^2}{4A_\perp}, \quad (4)$$
$$\delta\omega_{T_{\pm1}} \approx \pm\frac{\delta_z}{2}$$

It shows that the $|S_0\rangle$ and $|T_0\rangle$ states have zero first-order dependence on magnetic field, and the frequency fluctuation of the $|S_0\rangle \rightarrow |T_0\rangle$ (denoted as ST_0 hereinafter) transition is reduced to $\sim\delta^2/A$ (Fig. 1B). Therefore, a line-narrowing phenomenon will appear.

Correlation detection protocol for zero-field EPR spectroscopy

Such a narrowed ST_0 spectrum is challenging to observe by the previous microwave power-sweeping method (*12*), as it requires extreme power stability of the entire microwave circuits. The commonly used double electron-electron resonance (DEER) method (*5*–*10*) is also not suitable, because the interrogation time is limited by the coherence time T_2 of the NV center. Inspired by the correlation spectroscopy of nuclear spins (*16*), we develop a modified correlation detection protocol for zero-field EPR spectroscopy. Then, the sensor's lifetime can be increased to the spin-locking relaxation time $T_{1\rho}$, which is usually much longer than T_2 for shallow NV centers (*12*, *29*).

As shown in Fig. 2A, our pulse protocol consists of two zero-field DEER sequences (see Materials and Methods) separated by a spin-locking sequence. After initialization of the NV center in $|0\rangle$ state by a 532-nm laser excitation, a resonant microwave π pulse creates a superposition state $(|1\rangle + |-1\rangle)/\sqrt{2}$, which evolves during the first DEER period with an accumulated phase φ_1, and thus becomes $(e^{i\varphi_1}|1\rangle + e^{-i\varphi_1}|-1\rangle)/\sqrt{2}$. We rewrite it as $\cos\varphi_1 |\psi_+\rangle + i\sin\varphi_1 |\psi_-\rangle$, where $|\psi_\pm\rangle = (|1\rangle \pm |-1\rangle)/\sqrt{2}$. During the spin-locking period, both the $|\psi_+\rangle$ and $|\psi_-\rangle$ states can be locked by the continuous driving field, but the coherence between them vanishes, which can be regarded as an ensemble projection measurement (see Materials and Methods). In this period, we can perform any manipulations on the target spin, which determines the accumulated phase φ_2 during the second DEER period. If the NV state is projected to $|\psi_+\rangle$ (or $|\psi_-\rangle$) with probability of $\cos^2\varphi_1$ (or $\sin^2\varphi_1$) after the spin-locking period, the final state will be $\cos\varphi_2 |0\rangle + i\sin\varphi_2 |\psi_-\rangle$ (or $\sin\varphi_2 |0\rangle - i\cos\varphi_2 |\psi_-\rangle$) with the population of $|0\rangle$ read out by the photoluminescence (PL) rate of the NV center. The resulting correlation signal is given by

$$S_{corr} = \frac{1}{2}[1 + \langle\cos 2\varphi_1 \cos 2\varphi_2\rangle] \quad (5)$$

where the brackets denote statistical average.

Experimental demonstration of the high-resolution EPR spectroscopy

We perform the experiments on a coupled system of NV and P1 centers at zero magnetic field. We compensate for the residual magnetic field to ~0.01 G by three-dimensional Helmholtz coils (see Materials and Methods and fig. S1). P1 center is another kind of defect in diamond, consisting of only a substitutional nitrogen atom (*11*,*12*). The ^{15}N P1 center is an $S = 1/2$, $I = 1/2$ system, making it an ideal candidate for demonstrations of the high-resolution zero-field EPR spectroscopy. Both the NV and P1 centers are created by implantation of $^{15}N_2^+$ ions into a bulk diamond. With proper energy and dose (see Materials and Methods), the created NV centers can be well resolved by a home-built confocal microscope. For some NV centers, one can find a single adjacent P1 center by performing the zero-field DEER measurements (see section S2 and fig. S2). The hyperfine constants of ^{15}N P1 center are $A_\perp = 114$ MHz and $A_\parallel = 160$ MHz (*30*) and thus the expected transition frequencies of ST_0 and $ST_{\pm1}$ transitions are 114 and 137 MHz, respectively.

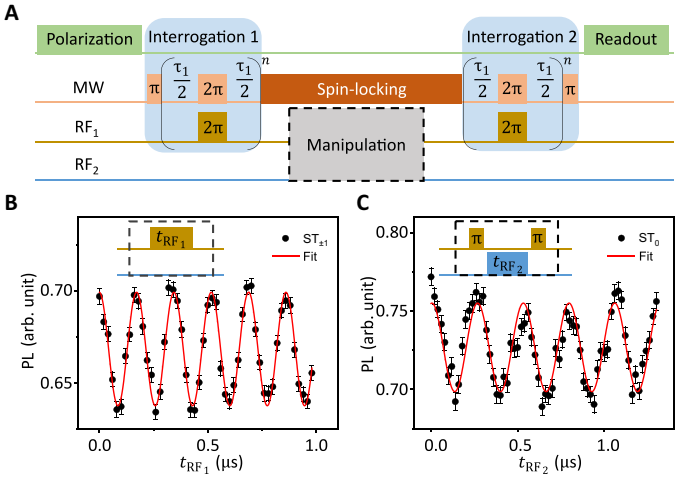

Fig. 2. Correlation protocol for EPR measurements. (**A**) Schematics of the pulse sequence. The interrogations are two DEER sequences ($n = 2$) for detections of the target spin state. The detected phase signal is stored on the populations of NV dressed states and protected by spin locking. The correlation signal depends on the manipulations on the target spin, which is denoted by the black dashed box. MW, microwave. (**B** and **C**) Rabi oscillations for the $ST_{\pm1}$ (B) and ST_0 (C) transitions. Insets give the corresponding manipulations on P1 centers. The spin-locking time is fixed to 10 μs. The red lines are sine fittings. Error bars indicate SEM. arb., arbitrary.

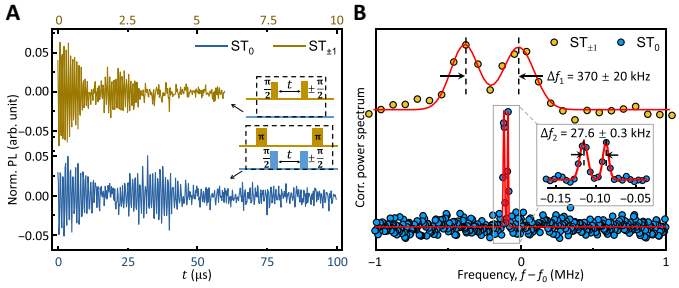

Fig. 3. High-resolution EPR spectroscopy of single P1 centers. (**A**) Correlation signals of Ramsey experiments for the $ST_{\pm1}$ (top) and ST_0 (bottom) transitions. Insets give the corresponding manipulations on P1 centers. Each experiment consists of two measurements, $\pi/2 \rightarrow -\pi/2$ and $\pi/2 \rightarrow \pi/2$, and the differential signal is presented. The top data have a 10× magnification in horizontal axis and still show faster decay. All the signals are undersampled, and the actual frequencies can be recovered with the prior knowledge of the rough resonance frequencies. (**B**) Fourier transformations of the time-domain data. The frequencies are relative to 137 MHz ($ST_{\pm1}$) and 114 MHz (ST_0). The points are experimental results, while the solid lines are two-Gaussian fittings. The fitting FWHM is 230±20 kHz (left) and 260±20 kHz (right) for the $ST_{\pm1}$ spectra and 11.6±0.6 kHz (left) and 8.6±0.4 kHz (right) for the ST_0 spectra.

The P1 center can be fully controlled by resonant radio frequency (RF) pulses and reliably read out by the correlation detection protocol. Considering that the orientation of P1 center jumps between the four kinds of N─C bonds (fig. S1B) due to the Jahn-Teller effect (*31*), we adjust the RF direction to the vertical direction of the diamond surface by moving the P1 center to the central area of the Ω-shape waveguide, so that the effective control-field strengths for the different oriented P1 centers are the same to simplify the control. Figure 2B shows the Rabi oscillation between $|S_0\rangle$ and $|T_{\pm1}\rangle$, by varying the RF pulse length during the spin-locking period. The spin-locking power, denoted by the corresponding Rabi frequency of the NV center, is 30 MHz, resulting in $T_{1\rho} \sim 150$ μs. As a comparison, T_2 is just 16 μs (fig. S3). This interrogation time can be further improved to T_1 (~milliseconds), although with compromise of signal contrast (see Materials and Methods). As described above, the ST_0 transition is insensitive to the magnetic field, and thus also insensitive to the coupling with the NV center. To observe this mute transition, we use $|T_{\pm1}\rangle$ as auxiliary states. As shown in Fig. 2C, we can also observe the Rabi oscillation between $|S_0\rangle$ and $|T_0\rangle$. The detailed calculations of these correlation Rabi measurements are in section S3.

To obtain the EPR spectra, we perform the Ramsey experiments on the P1 center. Specifically, for the $ST_{\pm1}$ transition, the manipulations during spin-locking period are two resonant π/2 RF pulses with varying separations t, as illustrated in Fig. 3A. Here, the RF pulses remain unchanged during the variation of t to avoid any spurious effect on the NV spin. Thus, the phase difference between them varies proportionally to t, resulting in oscillation signals (Fig. 3A). The Fourier transformation gives the resonance spectrum. The decay of the signal remarks the decoherence process, resulting in line broadening in the frequency domain. Similarly, the Ramsey experiment of the ST_0 transition can also be performed with the assistance of the $ST_{\pm1}$ transition, which shows a much slower decay. The detailed calculations of these correlation Ramsey measurements are in section S4. Figure 3B gives the Fourier transformation spectra and clearly shows the improvement of the spectral resolution. The Gaussian fittings give the linewidths [quoted as the full width at half maximum (FWHM)] of the spectra, the minimums of which are 230 ± 20 kHz and 8.6 ± 0.4 kHz for the $ST_{\pm1}$ and ST_0 transitions, respectively. The latter has (27 ± 3)–fold improvement. If the line broadening is solely induced by magnetic noises, the estimated improvement should be >130 (see Materials and Methods). This deviation suggests that other decoherence sources emerge when the magnetic noise is suppressed, such as electric or strain field noises (*32*).

Both of the spectra show clear line splitting, but the reasons are different. For the $ST_{\pm1}$ transition, the line splitting of 370 kHz is induced by the coupling with a nearby ^{13}C nuclear spin, which is widespread in natural-isotope diamonds. As a comparison, we repeat the measurements on a ^{12}C isotopically purified diamond, where the line splitting disappears but remains in the ST_0 spectrum (fig. S4). Actually, the ^{13}C coupling will not induce obvious splitting for the ST_0 transition because of the quadratic dependence on the magnetic field according to Eq. 4. A probable reason for the ST_0 line splitting is the existence of local electric or strain fields (*33*). Similar with donor electron spins in silicon (*21*, *34*), the hyperfine coupling of P1 centers should also depend on electric or strain fields. Given that the hyperfine coupling here is anisotropic with jumping orientations, up to four ST_0 lines can emerge in a local static electric or strain field. The observation of only two lines suggests that the field is along a symmetric direction, probably perpendicular to the surface, as reported in a recent paper (*35*). Different from the magnetic field, the electric or strain field induces the same-order frequency shifts of the ST_0 and $ST_{\pm1}$ transitions because both of them are linearly dependent on the hyperfine constants. Therefore, such weak couplings cannot be resolved by the $ST_{\pm1}$ spectrum or previous non–zero-field measurements.

To further investigate the spectral figure, we apply a small magnetic field B and observe the spectral variance. As shown in Fig. 4A, further splittings appear with increasing B, which suggests that the $ST_{\pm1}$ line splitting at zero field comes from the coupling with a two-level system (i.e., ^{13}C nuclear spin) rather than a local static magnetic

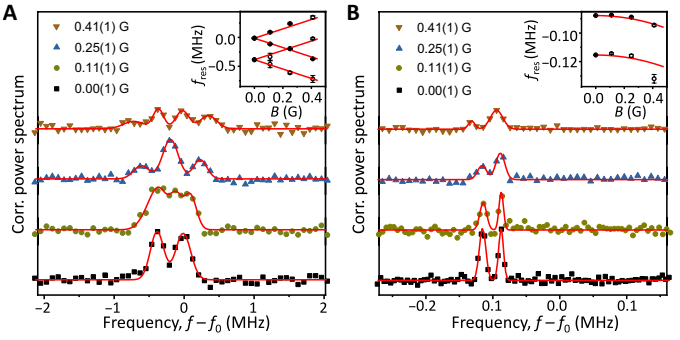

Fig. 4. Magnetic-field dependence of the line shape. The magnetic field *B* is applied along the vertical direction of the diamond surface, which is a symmetric direction of the four P1 axes. All the points are experimental data, fitted with *m*-Gaussian ($m = 2 - 4$) functions (solid lines). Insets give the fitting peak positions (f_{res}) versus magnetic fields with error bars defined by the fitting errors. (**A**) $ST_{\pm1}$ spectrum. Each peak at zero field splits independently with increasing *B*, and the expected splitting (solid lines in the inset) is calculated according to Eq. 4. (**B**) ST_0 spectrum. The two-peak pattern remains unchanged with increasing *B*, despite overall peak shifts and line broadening. Each group of peak positions (solid lines in the inset) is calculated according to Eq. 4.

field. On the other hand, the line shape of the ST_0 transition remains unchanged, despite the overall small shifts and line broadening (Fig. 4B). The line splitting is almost constant versus *B* but varies for different P1 centers (fig. S4), which suggests different local electric or strain environments (*33*). The resonance frequencies clearly show the linear and quadratic dependence on *B* for the $ST_{\pm1}$ and ST_0 transitions, respectively, which is well predicted by Eq. 4. The almost changeless peak positions in Fig. 4B also reveal the line-narrowing nature, which is degrading with increasing *B* because of the growing fluctuation of $(\gamma_e B + \delta)^2$.

DISCUSSION

In conclusion, we have presented a method for measuring EPR spectra with high spectral resolution by using a magnetic noise–insensitive singlet-triplet transition at zero magnetic field. The experiment demonstrates that the EPR linewidth of P1 centers could be reduced by more than one order of amplitude to several kilohertz, and then some weak nonmagnetic effects can be found. Our results show that, as a sensor for EPR spectroscopy, the NV center has the potential to simultaneously achieve high spatial and high spectral resolution.

The P1 centers in diamond are ideal systems for demonstrations of this technique, while practical applications require target spins external to the diamond surface. Although this line-narrowing phenomenon also exists in many other paramagnetic materials, such as ^{15}N nitroxide spin labels (*7*) and some transition ions (*25*, *26*), the observations with NV centers are more challenging. First, fast diffusions of the target spins will cancel their dipolar couplings with the NV sensor in the absence of external magnetic field, making the detections impossible. Thus, the sample should be solid or quasi-solid. Fortunately, the zero-field powder spectra do not have the inhomogeneous line-broadening issue (*12*, *24*–*26*). Second, the spectral improvement will degrade with increasing magnetic noise strength as $\sim\delta/A$ and will vanish when the noise strength δ is comparable to or even larger than the hyperfine constant *A*. It means that the coherence properties of the target spins should not be too worse relative to $1/A$. This may be a problem for the transition ions, whose coherence times are usually much worse than free-radical spin labels. Nevertheless, it is recently reported that, with proper synthetic design, the coherence times of some transition metal complexes can even approach milliseconds (*36*). Third, the current measurement is still time-consuming. The widely used nitroxide spin labels may be bleached during the strong laser illumination (*7*, *8*). A possible solution is improving the detection efficiency by implanting the spin-to-charge readout technique (*37*) or extending the lifetimes of spin labels by lowering the temperature and moving to a vacuum environment (*8*).

If successfully generalizing to external paramagnetic targets, this technique will benefit many EPR studies with substantially improved precision. For example, zero-field EPR spectroscopy is a powerful tool to unambiguously extract the hyperfine constants (*12*), which can reflect the local polarity profiles (*14*). By improving spectral resolution, more detailed microenvironment information can be explored. In addition, such magnetic field–insensitive singlet and triplet states can serve as a narrowband filter, which filters out magnetic fields of all frequencies except the one resonant with the transition. If considering dual spin targets in the presence of spin bath, all the target-environment spin dipolar couplings are killed, but the target-target coupling survives. Thus, the latter can be precisely detected by deploying our zero-field EPR technique, which offers interesting avenues for enhanced accuracy and detection range in distance measurement of spin-modified biomolecules (*15*).

MATERIALS AND METHODS

Experimental setup and diamond samples

The optical part of our setup is a home-built confocal microscopy, with a diode laser (CNI Laser MGL-III-532) used for illumination and an avalanche photodiode (Perkin Elmer SPCM-AQRH-14) used for photon collection. All the microwave and RF pulses are generated by an arbitrary waveform generator (Keysight M8190a) and amplified by two amplifiers accordingly (Mini-Circuits ZHL-16W-43+ and LZY-22+). The Ω-shape waveguide has a diameter of 50 μm with a radiation field perpendicular to the plane in the central area.

Two diamond samples are involved, denoted as diamonds A and B. Both of them are obtained commercially, 100-oriented, electronic grade, and implanted with $^{15}N_2^+$ ions. Diamond A is implanted with an energy of 30 keV and a dose of 3×10^{10} cm^{-2}. We fabricated nanopillars on diamond A to enhance the photon-collection efficiency (*38*). Diamond B has an extra growth layer with 99.9% ^{12}C isotopic purity. It is implanted with an energy of 5 keV and a dose of 1.7×10^{10} cm^{-2}. The simulated ion straggling (~7 nm for diamond A and ~4 nm for diamond B) is much smaller than the mean spacing of ions (~60 nm for diamond A and ~80 nm for diamond B), so the detected signal is dominated by a single P1 center arising from the adjacent nitrogen ion. The data in fig. S4 are measured on diamond B, and all the other data are measured on diamond A.

Compensation of residual magnetic field

The NV center can detect magnetic fields via optically detected magnetic resonance (ODMR) spectrum. In a small magnetic field ($\gamma_e B \ll D$), the line splitting is proportional to the component parallel to the N-V axis. However, the smallest resolvable magnetic field is limited by the ODMR linewidth. To reliably compensate for the residual magnetic field, we take advantage of the symmetric nature

of the ODMR spectrum versus magnetic fields. As shown in fig. S1A, with increasing currents applied to the coils, the ODMR linewidth first decreases and then increases. The symmetric center point marks the zero axial magnetic field. By using three differently oriented NV centers, the residual vector magnetic field **B** can be totally compensated. Figure S1B gives the schematics of the three NV centers, among which NV A/B and C are oriented perpendicular to the *X* and *Y* axis, respectively. We perform the compensation as follows: (i) Compensation of B_z. The ODMR linewidths of NV A and B are measured with sweeping *Z*-coil currents, and two symmetric center points $I_{Z,A}$ and $I_{Z,B}$ are recorded (fig. S1C). Then, the *Z*-coil compensation current is $I_Z = (I_{Z,A} + I_{Z,B})/2$ owing to the symmetry of NV A and B with respect to the *Z* axis. (ii) Compensation of B_y. Since the NV A and B are insensitive to B_x, the compensation of B_y is straightforward. As shown in fig. S1D, the symmetric center point is just the *Y*-coil compensation current. (iii) Compensation of B_x. Similar with (ii), the symmetric center point of NV C is just the *X*-coil compensation current (fig. S1E). The maximum fit error of the symmetric center point is 1 mA, while the stability of the power supplies is ~4 mA. The magnetic field linearly depends on the current with a coefficient of 2.8 G/A. Therefore, the magnetic field after compensation is estimated to be ~0.01 G.

Zero-field DEER

For NV center–based EPR, the DEER sequence is widely used for the detection of electron spins (*5*–*7*, *9*, *10*), where the NV center itself is also an electron spin (*S* = 1). Because of the degeneracy of $|\pm\rangle 1$ at zero magnetic field, the zero-field DEER sequence is slightly different (fig. S2). Specifically, a π pulse can flip the NV state from $|0\rangle$ to a superposition state $(|1\rangle + |-1\rangle)/\sqrt{2}$, which serves as an interferometer, and a 2π pulse can switch $|1\rangle$ and $|-1\rangle$, which is a decoupling operation. During the evolution, the superposition state accumulates a phase $\phi = a \cdot \tau$, where *a* is the dipolar coupling strength, and becomes $(e^{i\phi}|+1\rangle + e^{-i\phi}|-1\rangle)/\sqrt{2}$. Last, a second π pulse reverses this state back to $|0\rangle$ with the population $\cos^2\phi$ read out by the PL rate.

The dipole-dipole coupling between the sensor and the target can be approached by

$$H_{dd} \approx C(\mathbf{n}_{NV}, \mathbf{n}_{tar}, \mathbf{r})\, S_z^{NV} S_{zz}^{T} \tag{6}$$

where the coupling strength *C* depends on the orientations of the NV center $\mathbf{n}_{NV}$, the target spin $\mathbf{n}_{tar}$, and the spacing vector **r** between them. S_{zz}^{T} is a reduced spin operator of the target spin in the singlet-triplet basis $\{|T_{+1}\rangle, |S_0\rangle, |T_0\rangle, |T_{-1}\rangle\}$

$$S_{zz}^{T} = \frac{1}{2}\begin{pmatrix} 1 & & & \\ & 0 & & \\ & & 0 & \\ & & & -1 \end{pmatrix} \tag{7}$$

The detailed derivation process is in section S1. Now, one can directly see that the coupling will disappear if the target spin is in the $|S_0\rangle$ or $|T_0\rangle$ states, with a magnetic field–insensitive nature. Hence, the DEER measurement cannot directly capture the signal of the ST_0 transition. Otherwise, if the target spin is in the $|T_{\pm1}\rangle$ states, the coupling strength $a = \pm C/2$. Similar to the NV center, a π RF pulse will flip the target spin from $|S_0\rangle$ to a superposition state of $|T_{\pm1}\rangle$, while a 2π RF pulse will switch $|T_{+1}\rangle$ and $|T_{-1}\rangle$. The latter leads to a stronger equivalent coupling strength (fig. S2), which is more favorable in the presence of decoherence. As calculated in section S2, the zero-field DEER signal is

$$S(\tau) = \frac{3}{4} + \frac{1}{4} e^{-(\tau/T_{2,NV})^p} \cos C\tau \tag{8}$$

where the decoherence of the NV center is described by a stretched exponential decay, and *p* is in the range of 1 to 3 determined by the dynamic of bath (*39*).

Zero-field spin locking

The Hamiltonian of the NV center at zero magnetic field is

$$H_0 = DS_z^2 \tag{9}$$

where $S(S = 1)$ is the NV electron spin operators and *D* is the zero-field splitting. During the spin-locking period, we apply a phase-modulated microwave of the form (*40*)

$$H_1 = \Omega_1 \cos\left[Dt + \frac{2\Omega_2}{\Omega_1}\sin\Omega_1 t\right] S_x \tag{10}$$

where Ω_1 is the corresponding Rabi frequency and Ω_2 is the phase modulation strength. In this experiment, $\Omega_2 = 0.3\Omega_1$. By moving to the interaction picture, the Hamiltonian becomes

$$\begin{aligned} H_I &= e^{if(t)S_z^2}(H_0 + H_1)\, e^{-if(t)S_z^2} - f'(t)\, S_z^2 \\ &= \frac{\Omega_1}{2} S_x - 2\Omega_2 \cos\Omega_1 t\, S_z^2 \end{aligned} \tag{11}$$

where $f(t) = Dt + (2\Omega_2/\Omega_1)\sin\Omega_1 t$, and we ignore the high-frequency items. This is just the common Rabi model. Moving again to the second interaction picture and ignoring the high-frequency items, we can write

$$\begin{aligned} H_{II} &= e^{i\frac{\Omega_1 t}{2}S_x} H_I\, e^{-i\frac{\Omega_1 t}{2}S_x} - \frac{\Omega_1}{2} S_x \\ &= -\frac{\Omega_2}{2}(S_z^2 - S_y^2) \end{aligned} \tag{12}$$

For an initial state $|\psi(0)\rangle$, the evolution of the NV state can be written as

$$|\psi(t)\rangle = e^{-if(t)S_z^2} e^{-i\frac{\Omega_1}{2}S_x t} e^{-iH_{II}t} |\psi(0)\rangle \tag{13}$$

By choosing an integral-period evolution time, i.e., $t = k \cdot \frac{4\pi}{\Omega_1}, k = 1,2,\ldots$, the evolution is simplified to

$$|\psi(t)\rangle = e^{-iH_{II}t} |\psi(0)\rangle \tag{14}$$

where the phase item $\exp[-i\, DtS_z^2]$ is absorbed in the normal rotating reference frame. After the first DEER period, the NV state becomes $\cos\phi_1 |\psi_+\rangle + i \sin\phi_1 |\psi_-\rangle$. Note that both $|\psi_+\rangle$ and $|\psi_-\rangle$ are eigenstates of H_{II}, so the spin-locking process is just a free induction decay process in the interaction picture. The populations of $|\psi_\pm\rangle$ are protected while the coherence between them is destroyed by the environmental noise. Therefore, the NV state becomes a mixed state of $|\psi_+\rangle$ and $|\psi_-\rangle$ after the spin-locking period.

Alternative protocol for correlation detection

Alternatively, we can also avoid the spin-locking microwave in some further practical applications, such as sensing in a living cell, where long microwave pulses may be potentially harmful to biological tissues. This correlation protocol consists of two DEER sequence separated by a free evolution (fig. S5). Similar to the analysis in Correlation detection protocol for zero-field EPR spectroscopy, the NV state starts from $|0\rangle$ and becomes $\cos\varphi_1|0\rangle + i\sin\varphi_1|\psi_-\rangle$ after the first DEER period. During the free evolution, the coherence vanishes with NV state projecting to either $|0\rangle$ with a probability of $\cos^2\varphi_1 - 1/2\sin^2\varphi_1$, or a totally mixed state $(|0\rangle\langle 0| + |1\rangle\langle 1| + |-1\rangle\langle -1|)/3$ with a probability of $3/2\sin^2\varphi_1$. The former has a similar evolution to the first DEER period and becomes $\cos\varphi_2|0\rangle + i\sin\varphi_2|\psi_-\rangle$ after the second DEER period, while the latter has an idle evolution. Therefore, the correlation signal is

$$\begin{aligned} S_{\mathrm{corr}}(\varphi_1,\varphi_2) &= \left\langle \left(\cos^2\varphi_1 - \frac{1}{2}\sin^2\varphi_1\right)\cos^2\varphi_2 + \frac{1}{2}\sin^2\varphi_1 \right\rangle \\ &= \frac{1}{8}[3 + \langle\cos 2\varphi_1\rangle + \langle\cos 2\varphi_2\rangle + \langle 3\cos 2\varphi_1 \cos 2\varphi_2\rangle] \end{aligned} \tag{15}$$

Here, one can see that the signal contrast is reduced by 25%, which is the cost of removing the spin-locking microwave. Nevertheless, the limitation of interrogation duration can be further released to $T_{1,\mathrm{NV}}$.

Spectral linewidth analysis

According to Eq. 4, the fluctuations of the transition frequencies can be approached by

$$\begin{aligned} \delta\omega_{\mathrm{ST}_{\pm1}} &\approx \pm\frac{1}{2}\delta_z, \\ \delta\omega_{\mathrm{ST}_0} &\approx -\frac{A_\perp}{A_\parallel^2 - A_\perp^2}(\delta_x{}^2 + \delta_y{}^2) + \frac{1}{2A_\perp}\delta_z{}^2 \end{aligned} \tag{16}$$

For Ramsey measurements, the magnetic noise is dominated by the low-frequency component, which can be modeled as a quasi-static random variable characterized by a normal distribution

$$P(\delta = x) = \frac{1}{\sqrt{2\pi}\,\sigma} e^{-\frac{x^2}{2\sigma^2}} \tag{17}$$

with SD σ used to characterize the noise amplitude. Accordingly, the energy levels will fluctuate and can also be modeled as some kind of distributions, of which the SDs can be used to estimate the linewidth. According to Eq. 16, the SD of $\omega_{\mathrm{ST}\pm1}$ can be directly written as

$$\sigma_{\mathrm{ST}_{\pm1}} = \frac{1}{2}\sigma \tag{18}$$

Considering isotropic magnetic noise, i.e., $\sigma_x = \sigma_y = \sigma_z = \sigma$, the SD of $\omega_{\mathrm{ST}0}$ can be calculated as

$$\begin{aligned} \sigma_{\mathrm{ST}_0} &= \sqrt{\langle(\delta\omega_{\mathrm{ST}_0})^2\rangle - \langle\delta\omega_{\mathrm{ST}_0}\rangle^2} \\ &= \sigma^2\sqrt{\frac{4A_\perp^2}{(A_\parallel^2 - A_\perp^2)^2} + \frac{1}{2A_\perp^2}} \end{aligned} \tag{19}$$

where $\langle\bullet\rangle = \int\int\int \bullet\, P(\delta_x)P(\delta_y)P(\delta_z)d\delta_x d\delta_y d\delta_z$. Thus, the spectral-resolution improvement is estimated to be

$$\chi \sim \frac{\sigma_{\mathrm{ST}_{\pm1}}}{\sigma_{\mathrm{ST}_0}} = \left[\frac{64A_\perp^2}{(A_\parallel^2 - A_\perp^2)^2} + \frac{8}{A_\perp^2}\right]^{-\frac{1}{2}} \cdot (\sigma_{\mathrm{ST}_{\pm1}})^{-1} \tag{20}$$

For the data in Fig. 3, the linewidth of the $\mathrm{ST}_{\pm1}$ spectrum is 230 kHz, which is defined by the FWHM. Thus, $\sigma_{\mathrm{ST}_{\pm1}} = \mathrm{FWHM}/\sqrt{8\ln 2} \approx 98$ kHz, and $\chi \sim 130$. Actually, this improvement is underestimated because the distribution of the ST_0 transition is not Gaussian but a sharper type (fig. S6). The quadratic dependence on magnetic field is responsible to the asymmetric line shape. Both the disappearance of the asymmetric pattern and the degrading spectral-resolution improvement of the experimentally measured ST_0 spectrum suggest the existence of other decoherence resources. The magnetic noise can be increased by applying noise currents to the Helmholtz coils, and then the asymmetric pattern appears (fig. S6).

SUPPLEMENTARY MATERIALS

Supplementary material for this article is available at http://advances.sciencemag.org/cgi/content/full/6/22/eaaz8244/DC1

View/request a protocol for this paper from *Bio-protocol*.

REFERENCES AND NOTES

1. P. P. Borbat, A. J. Costa-Filho, K. A. Earle, J. K. Moscicki, J. H. Freed, Electron spin resonance in studies of membranes and proteins. *Science* **291**, 266–269 (2001).
2. Y. Artzi, Y. Twig, A. Blank, Induction-detection electron spin resonance with spin sensitivity of a few tens of spins. *Appl. Phys. Lett.* **106**, 084104 (2015).
3. D. Rugar, R. Budakian, H. J. Mamin, B. W. Chui, Single spin detection by magnetic resonance force microscopy. *Nature* **430**, 329–332 (2004).
4. S. Baumann, W. Paul, T. Choi, C. P. Lutz, A. Ardavan, A. J. Heinrich, Electron paramagnetic resonance of individual atoms on a surface. *Science* **350**, 417–420 (2015).
5. M. S. Grinolds, S. Hong, P. Maletinsky, L. Luan, M. D. Lukin, R. L. Walsworth, A. Yacoby, Nanoscale magnetic imaging of a single electron spin under ambient conditions. *Nat. Phys.* **9**, 215–219 (2013).
6. F. Shi, Q. Zhang, P. Wang, H. Sun, J. Wang, X. Rong, M. Chen, C. Ju, F. Reinhard, H. Chen, J. Wrachtrup, J. Wang, J. Du, Single-protein spin resonance spectroscopy under ambient conditions. *Science* **347**, 1135–1138 (2015).
7. F. Shi, F. Kong, P. Zhao, X. Zhang, M. Chen, S. Chen, Q. Zhang, M. Wang, X. Ye, Z. Wang, Z. Qin, X. Rong, J. Su, P. Wang, P. Z. Qin, J. Du, Single-DNA electron spin resonance spectroscopy in aqueous solutions. *Nat. Methods* **15**, 697–699 (2018).
8. L. Schlipf, T. Oeckinghaus, K. Xu, D. B. R. Dasari, A. Zappe, F. F. de Oliveira, B. Kern, M. Azarkh, M. Drescher, M. Ternes, K. Kern, J. Wrachtrup, A. Finkler, A molecular quantum spin network controlled by a single qubit. *Sci. Adv.* **3**, e1701116 (2017).
9. B. Grotz, J. Beck, P. Neumann, B. Naydenov, R. Reuter, F. Reinhard, F. Jelezko, J. Wrachtrup, D. Schweinfurth, B. Sarkar, P. Hemmer, Sensing external spins with nitrogen-vacancy diamond. *New J. Phys.* **13**, 055004 (2011).
10. H. J. Mamin, M. H. Sherwood, D. Rugar, Detecting external electron spins using nitrogen-vacancy centers. *Phys. Rev. B* **86**, 195422 (2012).
11. L. T. Hall, P. Kehayias, D. A. Simpson, A. Jarmola, A. Stacey, D. Budker, L. C. L. Hollenberg, Detection of nanoscale electron spin resonance spectra demonstrated using nitrogen-vacancy centre probes in diamond. *Nat. Commun.* **7**, 10211 (2016).
12. F. Kong, P. Zhao, X. Ye, Z. Wang, Z. Qin, P. Yu, J. Su, F. Shi, J. Du, Nanoscale zero-field electron spin resonance spectroscopy. *Nat. Commun.* **9**, 1563 (2018).
13. A. Martorana, G. Bellapadrona, A. Feintuch, E. Di Gregorio, S. Aime, D. Goldfarb, Probing protein conformation in cells by EPR distance measurements using Gd^{3+} spin labeling. *J. Am. Chem. Soc.* **136**, 13458–13465 (2014).
14. D. Kurad, G. Jeschke, D. Marsh, Lipid membrane polarity profiles by high-field EPR. *Biophys. J.* **85**, 1025–1033 (2003).
15. G. Jeschke, DEER distance measurements on proteins. *Annu. Rev. Phys. Chem.* **63**, 419–446 (2012).
16. A. Laraoui, F. Dolde, C. Burk, F. Reinhard, J. Wrachtrup, C. A. Meriles, High-resolution correlation spectroscopy of ^{13}C spins near a nitrogen-vacancy centre in diamond. *Nat. Commun.* **4**, 1651 (2013).
17. S. Zaiser, T. Rendler, I. Jakobi, T. Wolf, S.-Y. Lee, S. Wagner, V. Bergholm, T. Schulte-Herbrüggen, P. Neumann, J. Wrachtrup, Enhancing quantum sensing sensitivity by a quantum memory. *Nat. Commun.* **7**, 12279 (2016).
18. R. Sarkar, P. Ahuja, P. R. Vasos, G. Bodenhausen, Long-lived coherences for homogeneous line narrowing in spectroscopy. *Phys. Rev. Lett.* **104**, 053001 (2010).
19. J. J. Bollinger, J. D. Prestage, W. M. Itano, D. J. Wineland, Laser-cooled-atomic frequency standard. *Phys. Rev. Lett.* **54**, 1000–1003 (1985).
20. T. P. Harty, D. T. C. Allcock, C. J. Ballance, L. Guidoni, H. A. Janacek, N. M. Linke, D. N. Stacey, D. M. Lucas, High-fidelity preparation, gates, memory, and readout of a trapped-ion quantum bit. *Phys. Rev. Lett.* **113**, 220501 (2014).

21. G. Wolfowicz, A. M. Tyryshkin, R. E. George, H. Riemann, N. V. Abrosimov, P. Becker, H.-J. Pohl, M. L. W. Thewalt, S. A. Lyon, J. J. L. Morton, Atomic clock transitions in silicon-based spin qubits. *Nat. Nanotechnol.* **8**, 561–564 (2013).
22. K. J. Morse, P. Dluhy, J. Huber, J. Z. Salvail, K. Saeedi, H. Riemann, N. V. Abrosimov, P. Becker, H.-J. Pohl, S. Simmons, M. L. W. Thewalt, Zero-field optical magnetic resonance study of phosphorus donors in 28-silicon. *Phys. Rev. B* **97**, 115205 (2018).
23. M. Emondts, M. P. Ledbetter, S. Pustelny, T. Theis, B. Patton, J. W. Blanchard, M. C. Butler, D. Budker, A. Pines, Long-lived heteronuclear spin-singlet states in liquids at a zero magnetic field. *Phys. Rev. Lett.* **112**, 077601 (2014).
24. T. Cole, T. Kushida, H. C. Heller, Zero field electron magnetic resonance in some inorganic and organic radicals. *J. Chem. Phys.* **38**, 2915–2924 (1963).
25. L. E. Erickson, Electron-paramagnetic-resonance absorption by trivalent neodymium ions in single crystals of lanthanum trichloride and lanthanum ethyl sulphate in zero magnetic field. *Phys. Rev.* **143**, 295–303 (1966).
26. S. J. Strach, R. Bramley, EPR of the vanadyl ion in Tutton salts at zero magnetic field. *Chem. Phys. Lett.* **109**, 363–367 (1984).
27. R. Bramley, S. J. Strach, Electron paramagnetic resonance spectroscopy at zero magnetic field. *Chem. Rev.* **83**, 49–82 (1983).
28. H. Zheng, J. Xu, G. Z. Iwata, T. Lenz, J. Michl, B. Yavkin, K. Nakamura, H. Sumiya, T. Ohshima, J. Isoya, J. Wrachtrup, A. Wickenbrock, D. Budker, Zero-field magnetometry based on nitrogen-vacancy ensembles in diamond. *Phys. Rev. Appl.* **11**, 064068 (2019).
29. T. Rosskopf, A. Dussaux, K. Ohashi, M. Loretz, R. Schirhagl, H. Watanabe, S. Shikata, K. M. Itoh, C. L. Degen, Investigation of surface magnetic noise by shallow spins in diamond. *Phys. Rev. Lett.* **112**, 147602 (2014).
30. W. V. Smith, P. P. Sorokin, I. L. Gelles, G. J. Lasher, Electron-spin resonance of nitrogen donors in diamond. *Phys. Rev.* **115**, 1546–1552 (1959).
31. G. Davies, The Jahn-Teller effect and vibronic coupling at deep levels in diamond. *Rep. Prog. Phys.* **44**, 787–830 (1981).
32. M. Kim, H. J. Mamin, M. H. Sherwood, K. Ohno, D. D. Awschalom, D. Rugar, Decoherence of near-surface nitrogen-vacancy centers due to electric field noise. *Phys. Rev. Lett.* **115**, 087602 (2015).
33. T. Mittiga, S. Hsieh, C. Zu, B. Kobrin, F. Machado, P. Bhattacharyya, N. Z. Rui, A. Jarmola, S. Choi, D. Budker, N. Y. Yao, Imaging the local charge environment of nitrogen-vacancy centers in diamond. *Phys. Rev. Lett.* **121**, 246402 (2018).
34. F. R. Bradbury, A. M. Tyryshkin, G. Sabouret, J. Bokor, T. Schenkel, S. A. Lyon, Stark tuning of donor electron spins in silicon. *Phys. Rev. Lett.* **97**, 176404 (2006).
35. D. A. Broadway, N. Dontschuk, A. Tsai, S. E. Lillie, C. T.-K. Lew, J. C. McCallum, B. C. Johnson, M. W. Doherty, A. Stacey, L. C. L. Hollenberg, J.-P. Tetienne, Spatial mapping of band bending in semiconductor devices using in situ quantum sensors. *Nat. Electronics* **1**, 502–507 (2018).
36. J. M. Zadrozny, J. Niklas, O. G. Poluektov, D. E. Freedman, Millisecond coherence time in a tunable molecular electronic spin qubit. *ACS Cent. Sci.* **1**, 488–492 (2015).
37. B. J. Shields, Q. P. Unterreithmeier, N. P. de Leon, H. Park, M. D. Lukin, Efficient readout of a single spin state in diamond via spin-to-charge conversion. *Phys. Rev. Lett.* **114**, 136402 (2015).
38. B. J. M. Hausmann, T. M. Babinec, J. T. Choy, J. S. Hodges, S. Hong, I. Bulu, A. Yacoby, M. D. Lukin, M. Lončar, Single-color centers implanted in diamond nanostructures. *New J. Phys.* **13**, 045004 (2011).
39. N. Bar-Gill, L. M. Pham, C. Belthangady, D. Le Sage, P. Cappellaro, J. R. Maze, M. D. Lukin, A. Yacoby, R. Walsworth, Suppression of spin-bath dynamics for improved coherence of multi-spin-qubit systems. *Nat. Commun.* **3**, 858 (2012).
40. I. Cohen, N. Aharon, A. Retzker, Continuous dynamical decoupling utilizing time-dependent detuning. *Fortschr. Phys.* **65**, 1600071 (2017).

Acknowledgments: We thank R.-B. Liu for helpful discussions. **Funding:** This work was supported by the National Key Research and Development Program of China (grant nos. 2018YFA0306600 and 2016YFA0502400), the National Natural Science Foundation of China (grant nos. 81788101, 91636217, 11722544, 11761131011, and 31971156), the CAS (grants nos. GJJSTD20170001, QYZDY-SSW-SLH004, and YIPA2015370), the Anhui Initiative in Quantum Information Technologies (grant no. AHY050000), the CEBioM, the National Youth Talent Support Program, the Fundamental Research Funds for the Central Universities, the China Postdoctoral Science Foundation (grant no. BX20180294), and USTC Research Funds of the Double First-Class Initiative (grant no. YD2340002004). **Author contributions:** J.D. and F.S. supervised the entire project. F.K., F.S., and J.D. conceived the experiments. P.Z. and F.K. prepared the setup and performed the experiments, together with Z.Q. and Z.W. P.Y. and M.W. performed the ion implantation and nanofabrication. F.K. and Z.H. carried out the calculations. F.K., P.Z., and F.S. wrote the manuscript. All authors analyzed the data, discussed the results, and commented on the manuscript. **Competing interests:** The authors declare that they have no competing interests. **Data and materials availability:** All data needed to evaluate the conclusions in the paper are present in the paper and/or the Supplementary Materials. Additional data related to this paper may be requested from the authors.

Submitted 11 October 2019
Accepted 20 March 2020
Published 27 May 2020
10.1126/sciadv.aaz8244

Citation: F. Kong, P. Zhao, P. Yu, Z. Qin, Z. Huang, Z. Wang, M. Wang, F. Shi, J. Du, Kilohertz electron paramagnetic resonance spectroscopy of single nitrogen centers at zero magnetic field. *Sci. Adv.* **6**, eaaz8244 (2020).

Science Advances

Kilohertz electron paramagnetic resonance spectroscopy of single nitrogen centers at zero magnetic field

Fei Kong, Pengju Zhao, Pei Yu, Zhuoyang Qin, Zhehua Huang, Zhecheng Wang, Mengqi Wang, Fazhan Shi and Jiangfeng Du

Sci Adv **6** (22), eaaz8244.
DOI: 10.1126/sciadv.aaz8244